

# Aeroelastic Energy Harvesting: A Case for Galloping

Sandip Thakur <sup>a</sup>, Kamal Darlami <sup>b</sup>, Laxman Poudel <sup>c</sup>

<sup>a, b, c</sup> Department of Mechanical Engineering, Pulchowk Campus, IOE, TU, Nepal

Corresponding Email: <sup>a</sup> 074msmde017.sandip@pcampus.edu.np, <sup>b</sup> darlami.kd@pcampus.edu.np, <sup>c</sup> laxman@ioe.edu.np

## Abstract

Energy Harvesting (EH) from transverse galloping of bluff bodies can be used to convert wind energy into electrical power to develop self powered devices (like sensors). This paper focuses on the numerical investigation of flow induced vibration based energy harvesting by the use of piezoelectric material. Two way coupled fluid structure interaction simulation is carried out to get the displacement of a square base prism and the result is used to calculate the power produced. A maximum power output of 2.1 *mW* is predicted at a wind velocity of 12 *m/s*.

## Keywords

Energy Harvesting, Galloping, Quasi-Steady, Piezoelectric, Two-way Fluid Structure Interaction

## 1. Introduction

Energy harvesting also known as Power harvesting or energy scavenging is the process of capturing minute amount of energy (light, thermal, or kinetic energy) from one or more of the surrounding energy sources and transforming to a usable form of energy with the ultimate objective of developing self-powered sensors, Micro Electromechanical Systems (MEMS) or actuators, and other devices which can be achieved using either electromagnetic, electrostatic or piezoelectric transduction mechanisms [1].

Galloping is a velocity dependent, damping-controlled instability, giving rise to transverse or torsional motions involving low frequency, large-amplitude oscillations normal to the direction of incident wind. A. Barrero-Gil *et al.* [2] analyzed theoretically the feasibility of using transverse galloping phenomenon to extract energy from a fluid flow which occurs in some elastic bluff bodies when the velocity of the incident flow exceeds a certain critical value.

In galloping, the major limitation is the representation of the galloping aerodynamic loads [1]. Also, a better investigation is required to determine the effect of nonlinearities on the performance of the harvester.

Den Hartog [3] studied and explained the phenomenon of galloping for the first time in 1943. He used the quasi-steady hypothesis to describe the aerodynamic

forces and introduced a criterion for galloping stability of a structure. Generally, the transverse galloping of elastic bluff bodies takes place when the wind speed exceeds a critical value at which instability is initiated and the bluff body starts to oscillate.

In this research, the numerical investigation of flow induced vibration based energy harvesting is carried out. With the current rapid development of the Internet of Things (IoTs), energy harvesting offers significant advantages and opportunities to the development and application for smart cities, smart homes, smart health, smart agriculture, intelligent transportation, industry, security, marine, and so on.

## 2. Methodology

### 2.1 Physical Mechanism of Galloping

Figure (1) shows a spring supported model exposed to a steady flow of velocity  $U$  and density  $\rho$ . The spring has stiffness  $k$  per unit length. The steady fluid dynamic forces on the section are the drag force and the lift force per unit length given as,

$$F_D = \frac{1}{2}\rho U_{rel}^2 DC_D \quad F_L = \frac{1}{2}\rho U_{rel}^2 DC_L \quad (1)$$

Here, the width  $D$  is a dimension used as a reference to non-dimensionalize the lift and drag aerodynamic coefficients  $C_L$  and  $C_D$ . When the model translates downward, the angle of the flow relative to the mode is given by Equation (2),

$$\alpha = \arctan(\dot{y}/U) \quad (2)$$

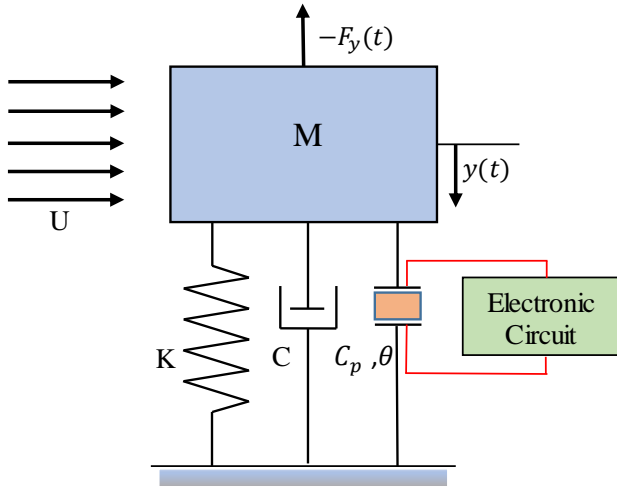


Figure 1: One-degree-of-freedom galloping model.

The equation of motion for the spring-supported, damped model including the piezoelectric transducer and considering a load resistance in the electrical circuit is [4],

$$m(\ddot{y} + 2\zeta\omega_N\dot{y} + \omega_N^2y) = F_y = 1/2\rho U^2 DC_y \quad (3)$$

$$C_p\dot{V} + \frac{V}{R} + \theta\dot{y} = 0$$

For small angles of attack,  $\alpha$ ,  $U_{rel}$  and  $C_y$  can be expanded in power

$$\alpha = \frac{\dot{y}}{U} + O(\alpha^2)$$

$$U_{rel} = U + O(\alpha^2)$$

$$C_y(\alpha) = C_{y|\alpha=0} + \left. \frac{\partial C_y}{\partial \alpha} \right|_{\alpha=0} \alpha + O(\alpha^2) \quad (4)$$

$$= -C_{L|\alpha=0} - \left[ \left. \frac{\partial C_L}{\partial \alpha} + C_D \right]_{\alpha=0} \alpha + O(\alpha^2)$$

Now from Equation (3) and (4) the net damping factor of vertical motion which is the sum of structural and aerodynamic components can be determined as [5],

$$\zeta_T = \zeta - \frac{\rho U D}{4m\omega_N} \left. \frac{\partial C_y}{\partial \alpha} \right|_{\alpha=0} \quad (5)$$

Unstable oscillations, i.e., galloping, occur when the effective damping of the system becomes negative. Thus, the model will be unstable if  $\frac{\partial C_y}{\partial \alpha} > 0$  or equivalently  $\frac{\partial C_L}{\partial \alpha} + C_D < 0$  which is known as the (Den Hartog, 1956) criterion and can be used to estimate when galloping will occur on any given

structure [3]. The critical velocity for onset of plunge galloping instability can be determined by setting  $\zeta_T$  to zero.

$$U_{crit} = \left( \frac{4m\omega_N\zeta}{\rho D} \right) / \left( \frac{\partial C_y}{\partial \alpha} \right) \quad [5] \quad (6)$$

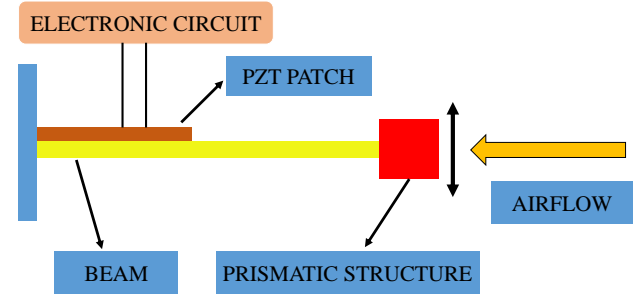


Figure 2: Schematic of a galloping based piezoelectric energy harvester [6]

## 2.2 Mathematical Modeling

The Navier-Stokes equations governs the fluid flow. This governing equation is derived from the laws of conservation of the mass, momentum, and energy which can be written as below

$$\frac{\partial \rho}{\partial t} + \Delta \cdot (\rho \vec{V}) = 0 \quad (7)$$

$$\frac{\partial}{\partial t} (\rho \vec{V}) + \Delta \cdot (\rho \vec{V} \vec{V}) = -\Delta P + \Delta \cdot (\vec{\tau}) + \rho \vec{g} + \vec{F}$$

Where,  $P$  is the static pressure,  $\vec{\tau}$  is the stress vector and  $\rho \vec{g}$ ,  $\vec{F}$  are the gravitational body force and the external forces. The stress tensor vector is given by,

$$\vec{\tau} = \mu \left[ (\Delta \vec{V} + \Delta \vec{V}^T) - \frac{2}{3} \Delta \cdot \vec{V} I \right]$$

### 2.2.1 Realizable $k$ - $\epsilon$ (RKE) Model

The  $k$ - $\epsilon$  model is a two equation turbulence model, holding two more additional transport equations (one for turbulent kinetic energy ( $k$ ) and one for turbulence dissipation rate ( $\epsilon$ ) to be solved.

The transport equations for  $k$  and  $\epsilon$  in the realizable  $k$ - $\epsilon$  model are [7]

$$\frac{\partial}{\partial t} (\rho k) + \frac{\partial}{\partial x_j} (\rho k u_j) = \frac{\partial}{\partial x_j} \left[ \left( \mu + \frac{\mu_t}{\sigma_k} \right) \frac{\partial k}{\partial x_j} \right] + E \quad (8)$$

$$\frac{\partial}{\partial t} (\rho \epsilon) + \frac{\partial}{\partial x_j} (\rho \epsilon u_j) = \frac{\partial}{\partial x_j} \left[ \left( \mu + \frac{\mu_t}{\sigma_\epsilon} \right) \frac{\partial \epsilon}{\partial x_j} \right] + Q$$

where,

$$E = G_k + G_b - \rho \epsilon - Y_M + S_k$$

$$Q = C_{1\epsilon} \frac{\epsilon}{k} C_{3\epsilon} G_b + \rho C_{1\epsilon} S_\epsilon - \frac{C_{2\rho} \rho \epsilon^2}{k + \sqrt{v\epsilon}} + S_\epsilon$$

### 2.3 Two-way Coupling

Two-way coupling is applied to the problem where the motion of a fluid influences a solid structure and at the same time the fluid field is influenced by the reaction of a solid structure [8]. In two-way-coupling calculations, the displacement of the structure is also transferred to the fluid solver.

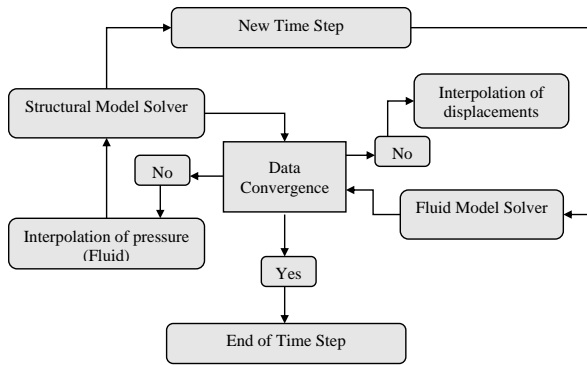


Figure 3: Two way coupling flow chart

### 2.4 Quasi-Steady Aerodynamics

Galloping is one particular example of flow-induced vibration problem, where the oscillation of the body are characterized by a timescale much larger than the characteristic timescale of the flow. A quasi-steady hypothesis for the aerodynamic character of the flow can be justified. This assumption of quasi-steady aerodynamics can be simplified neglecting unsteady terms.

### 2.5 Piezoelectricity

The electromechanical phenomenon in piezoelectric materials occurs when a coupling of electrical and mechanical states due to an applied mechanical stress. The governing piezoelectric constitutive equation for direct and converse piezoelectric effects are given by [9]

$$\begin{bmatrix} \delta \\ D \end{bmatrix} = \begin{bmatrix} S^E & s^t \\ d & \epsilon^T \end{bmatrix} \begin{bmatrix} \sigma \\ E \end{bmatrix} \quad (9)$$

## 3. Numerical Simulations

Firstly, the geometric models of both fluid domain and the structural solid are created using SolidWorks 2016. Then, the mesh of the fluid domain is created using ANSYS ICEM and the structural mesh is generated by using ANSYS Meshing tool. The fluid domain mesh differs with the structural mesh with parameters such as mesh resolution and cell size. After that, the two

computational meshes are imported to the respective numerical solvers (i.e. FLUENT and Transient Structural) in which the simulation setup is carried out. The solvers include the setup such as assigning properties of fluid and structure, allocating boundary conditions, setting the numerical schemes, etc. The structural model consists a square cylindrical member having elastic support and damping. Finally, System Coupling which exchanges the data is used to couple the two solvers in Workbench.

### 3.1 Geometry

The fluid domain is a rectangular prism in which the square cylindrical member of cross section  $40\text{ mm} \times 40\text{ mm}$  is placed inside. Figure (4) shows the geometry of the entire fluid domain. The structural member is placed in the middle at a distance of 180 mm from the inlet of fluid domain. The vertical and horizontal dimension of the fluid domain is taken as  $600\text{ mm}$  and  $1200\text{ mm}$  respectively.

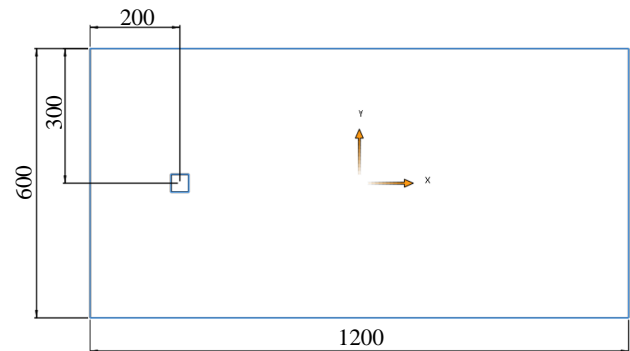


Figure 4: Geometry of fluid domain

### 3.2 Computational Mesh

ANSYS ICEM meshing tool is used for creating the computational mesh of the fluid domain. As the geometry is simple, the structured mesh is made up of quad cells. The total number of elements are 87,978. Figure (5) shows the entire computational fluid domain mesh.

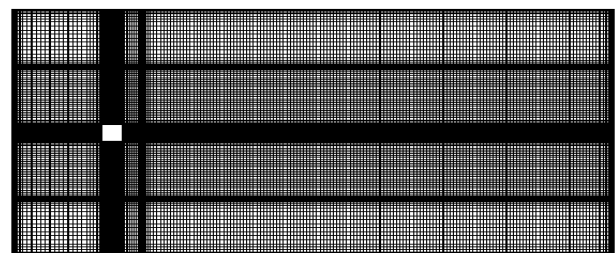


Figure 5: Computational mesh of the fluid domain

Figure (6) is the mesh independence test which shows that a mesh element of 87,500 i.e., 57,000 nodes are sufficient to ensure an accuracy of  $\pm 0.006$ . With increasing number of nodes from 11,652 to 27,204 the value of  $\overline{C_D}$  increases drastically as the coarse mesh is not fine enough to capture all the flow features. So, the mesh density should be increased. After further increasing number of nodes from 57,000 the value of  $\overline{C_D}$  doesn't change significantly ensuring it has reached mesh independence.

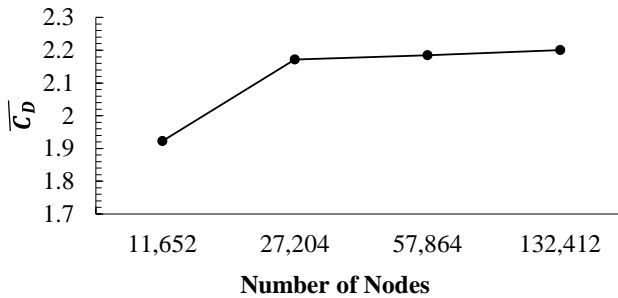


Figure 6: Spatial convergence of drag coefficient

### 3.3 Simulation Setup

The computational work of this research is divided into two parts, the first part deals with the CFD model and the other with the structural model.

#### 3.3.1 Material Properties

The fluid model is comprised of gas (air). The important properties of air and structural member used in this simulation are shown in Table (1) and Table (2) respectively.

Table 1: Material properties of air

Material	Density( $\rho$ )	Dynamic viscosity
Air	1.225 kg/m <sup>3</sup>	1.789 * 10 <sup>-8</sup> kg/ms

Table 2: Material properties of structural member

Material	$\rho$ (kg/m <sup>3</sup> )	Young's Modulus	$\mu$
Aluminum	2700	69GPa	0.3

#### 3.3.2 Boundary Conditions

Considering the experimental constraints of wind tunnel available in Pulchowk Campus, Institute of Engineering (IOE) whose maximum achievable velocity is 12 m/s, velocity inlet of 12 m/s is applied in x-direction and outlet is exposed to atmospheric pressure. In the case of two-way coupling, *dynamic mesh* settings have to be added in order to get a mesh

deformation in which the important step is to assign dynamic mesh zones among the boundaries of a fluid model. Here, all the symmetric boundaries are assigned to the *deforming* type of dynamic mesh zones, whereas the Square cylinder wall is allotted to the *System Coupling* type.

#### 3.3.3 Solver Setup

Table (3) lists the type of temporal and spatial discretization schemes used in Fluent.

Table 3: Discretization scheme used in Fluent

Temporal discretization	1 <sup>st</sup> order implicit
Pressure-Velocity Coupling	Coupled
Step Size	0.0001 sec
Gradient	Least square cell based
Pressure	2 <sup>nd</sup> order
Momentum	2 <sup>nd</sup> order upwind
Turbulence Model	Realizable $k - \epsilon$ Model
Kinetic energy (k)	1 <sup>st</sup> order upwind
Dissipation rate ( $\epsilon$ )	1 <sup>st</sup> order upwind

#### 3.3.4 ANSYS Mechanical Setup

The setup work consists of defining the boundary conditions, loads and analysis settings. The bottom and top surface of the square cylinder are connected to elastic support of stiffness 100 N/m and the surface of the cylinder is assigned as a *fluid solid interface* upon which the calculated fluid forces are applied. Beside this, it has the identical transient setups as assigned in Fluent setup.

## 4. Results and Discussion

### 4.1 CFD Results

Computational Fluid Dynamics (CFD) simulations of 2D geometry with unit cell thickness have been performed whose both side wall is assigned as symmetry in boundary condition. Figure (7) shows the pressure contour variation with time. The stagnation point of the flow is located at the front side of the square which leads to a high pressure difference in horizontal direction. Also, at the same time, flow starts to separate from the upper and lower side of the structure. It has global minimum pressure of -190 Pa and maximum pressure of 112.248 Pa. The pressure starts to decrease in a steady way towards the downstream.

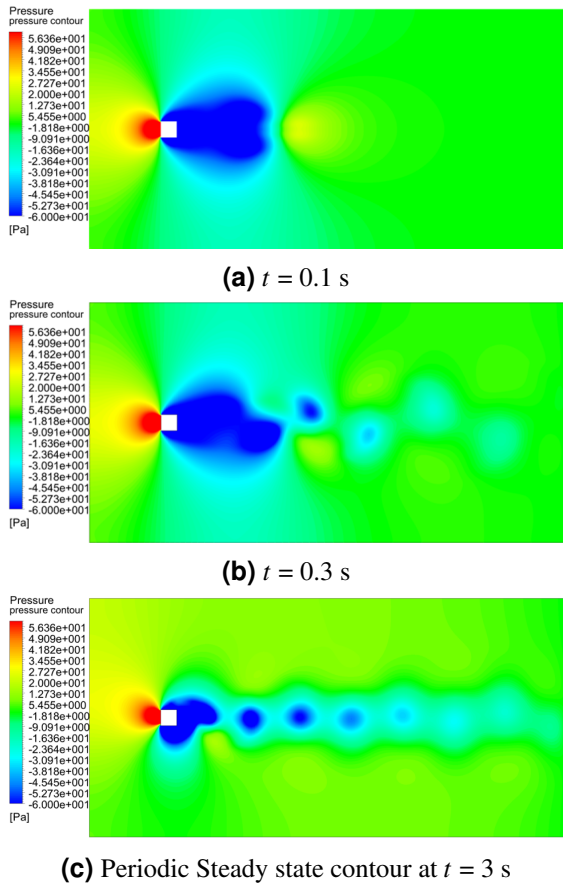


Figure 7: Pressure contour at different time-steps

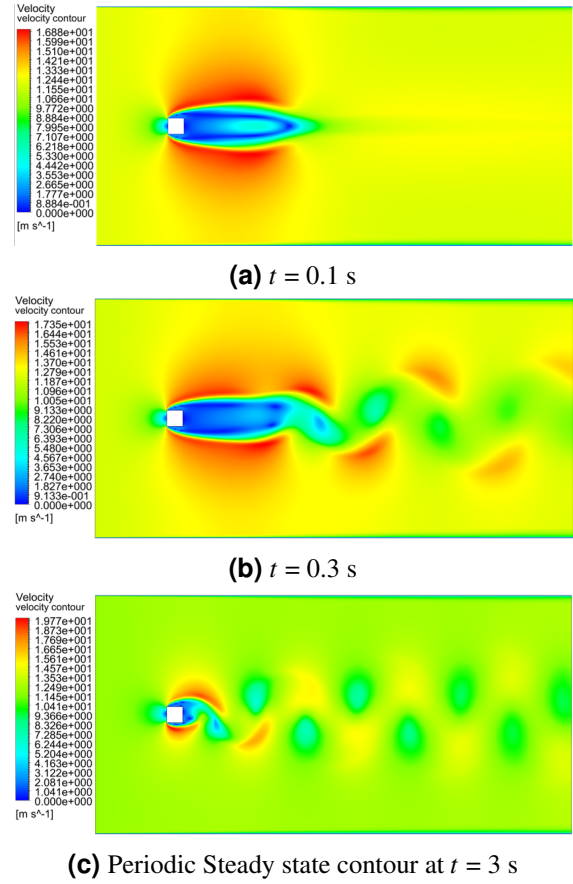


Figure 9: Velocity contour at different time-steps

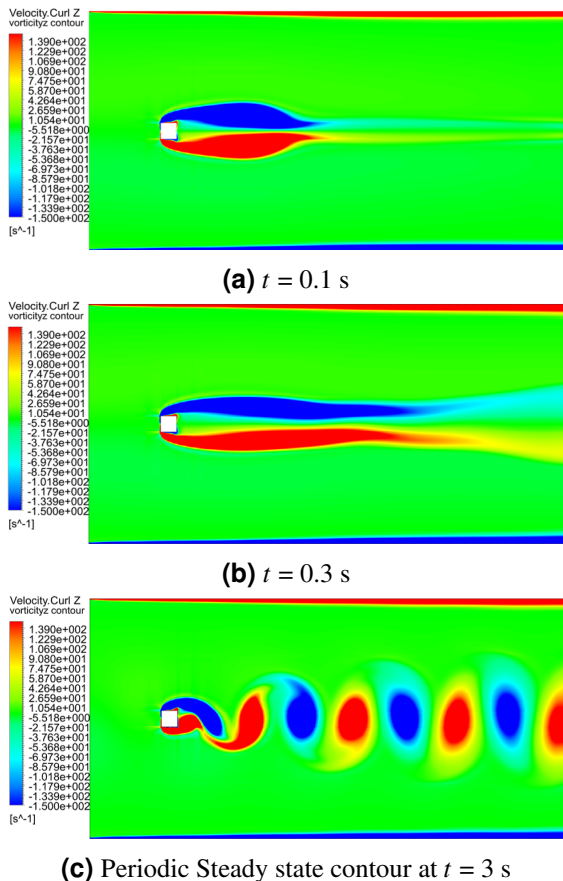


Figure 8: Vorticity Z contour at different time-steps

Figure (8) shows the development of Von Karman Street with time. The vorticity field is developed due to the velocity in y-direction which is found to be  $11.089 \text{ m/s}$  in negative y-direction and  $11.091 \text{ m/s}$  in positive y-direction. The maximum and minimum vorticity z field is found to be  $7600.4 \text{ s}^{-1}$  and  $-5636.62 \text{ s}^{-1}$ . The periodic vorticity field is in accordance with the vorticity field of Joly *et al.* [10]

Figure (9) shows the velocity contour at different time step. The flow separates from the upper and lower side of the structure and starts to oscillate in the wake region after 0.2 secs. In the region just after the flow separation maximum velocity of  $19.17 \text{ m/s}$  is attained.

#### 4.2 Drag and Lift Coefficient Vs Flow Time

Figure (10) and Figure (11) shows the lift and drag coefficient vs flow time at periodic steady state respectively. The mean coefficient of drag is found to be 2.185 which agrees with the corresponding numerical data.

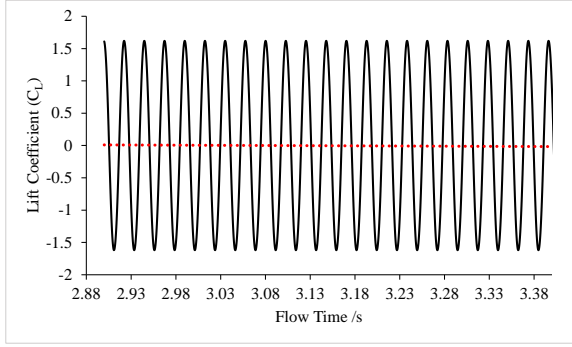


Figure 10: Lift coefficient Vs Flow time

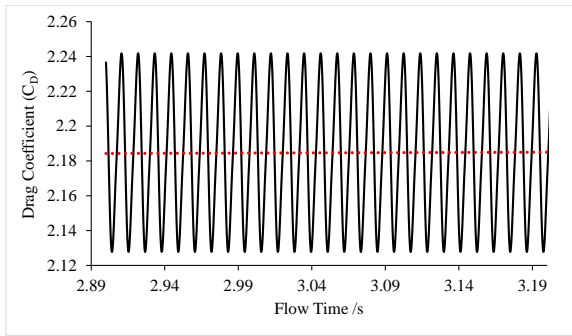


Figure 11: Drag coefficient Vs Flow time

### 4.3 Fluid Structure Interaction (FSI) Results

Two way FSI simulations have been performed to predict the tip displacement attached to cantilever beam. Figure (12) shows the predicted tip displacement. The amplitude of the tip displacement increases with time and then reaches a constant value. The maximum amplitude predicted is approximately 50.4 mm which is considerable for the beam of length 170 mm.

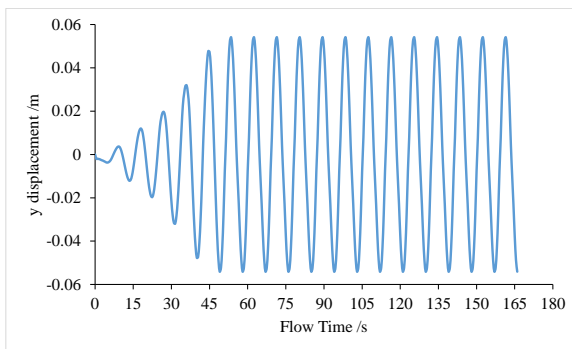


Figure 12: Tip Displacement Vs Flow time

Two PZT-5A type piezoelectric sheets having electro-mechanical coupling term  $\theta = 1.55 \text{ mN/V}$  and the equivalent capacitance of  $C_p = 120 \text{ nF}$  [11] are used in the analysis to predict the voltage generated due to tip displacement.

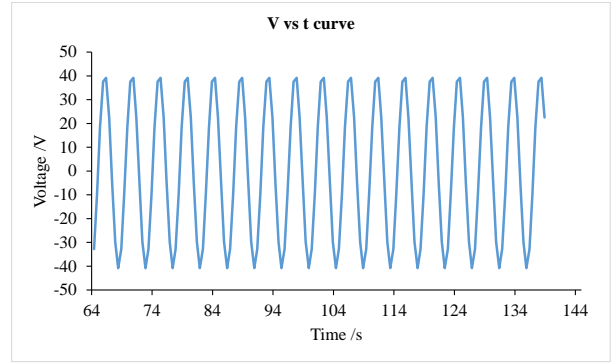


Figure 13: Voltage generated by piezoelectric sheets at steady state,  $0.7 \text{ M}\Omega$  load resistance

The output voltage predicted by solving Equation (3) at a wind velocity of  $12 \text{ m/s}$  and across a load resistance of  $0.7 \text{ M}\Omega$  at steady state is shown in Figure (13). The maximum steady state voltage of  $38 \text{ V}$  is predicted and the peak output power ( $P = V_{peak}^2 / R_L$ ), where  $V_{peak}$  is the peak Voltage across load resistance ( $R_L$ ) is found to be  $2.1 \text{ mW}$ .

### 4.4 Validation and Comparison of Results

Table (4) summarizes the various global parameters such as the dimensionless shedding frequency ( $StrouhalnumberSt = f \frac{D}{U}$ ), where,  $f$  is the vortex shedding frequency,  $D$  is the square-cylinder side and  $U$  is the reference velocity assumed at the inlet of the domain, the time mean drag coefficient  $\overline{C_D}$  and the time mean lift coefficient  $\overline{C_L}$ . All these parameters are calculated by averaging the last 20 steady vortex shedding cycles of the simulation. The Strouhal number is slightly greater than experimental data but they have a similar accuracy as the numerical data. The disagreements are due to differences in boundary conditions mainly wall law or damping functions used around the square cylinder.

Table 4: Comparison of global parameters

Reference	$\overline{C_L}$	$\overline{C_D}$	(St)
Numerical data:			
[12]	0.005	2.09	0.133
[13]	-0.02	2.2	0.13
[14]	-0.05	2.05	0.131
[15]	0.0093	2.62	0.131
[16]	0.01	2.72	0.16
Exp. data: [17, 18]	-	2.1	0.132
This work	-0.035	2.185	0.138

Also, the predicted steady state voltage in Figure (13)

is in close agreement with that of Sirohi and Mahadik [19].

## 5. Conclusion

A theoretical spring supported damped model representing the dynamics of transverse motion of a system coupled to a purely resistive energy harvesting circuit has been considered. This study has illustrated the numerical investigation of aeroelastic energy harvesting based on galloping phenomenon at a wind velocity of 12 *m/s* and across a load resistance of 0.7 *MΩ*. The CFD simulation results are compared with the corresponding numerical and experimental data which validates the CFD simulation and the tip displacement result obtained from FSI simulation is used to predict the amount of energy that could be harvested. A peak output power of 2.1 mW is predicted which is sufficient to power small sensor.

## 6. Future Works

Although the quasi-steady approximation is considered in the research, proper development of unsteady flow representation is required for higher velocities in order to determine the galloping force. A parametric study can be performed to ascertain the effects of the mechanical parameters and the electrical load resistance across piezoelectric on the energy harvesting performance to improve the output power from galloping phenomenon. Also, an experimental study is recommended for validation and improvement of research.

## Acknowledgments

The authors would like to thank University Grants Commission (UGC) for providing the financial support to complete this research. Also, the authors would like to acknowledge the support of Department of Mechanical and Aerospace Engineering for providing the necessary platform and computational resources for carrying out the work.

## References

- [1] Abdessattar Abdelkefi. Aeroelastic energy harvesting: A review. *International Journal of Engineering Science*, 100:112–135, 2016.
- [2] Antonio Barrero-Gil, G Alonso, and A Sanz-Andres. Energy harvesting from transverse galloping. *Journal of Sound and Vibration*, 329(14):2873–2883, 2010.
- [3] JP Den Hartog. *Mechanical vibrations* (1956). *McGrawHill Book Company*, 1985.
- [4] A Abdelkefi, MR Hajj, and AH Nayfeh. Piezoelectric energy harvesting from transverse galloping of bluff bodies. *Smart Materials and Structures*, 22(1):015014, 2012.
- [5] Michael P Paidoussis, Stuart J Price, and Emmanuel De Langre. *Fluid-structure interactions: cross-flow-induced instabilities*. Cambridge University Press, 2010.
- [6] Hassan Elahi, Marco Eugeni, and Paolo Gaudenzi. A review on mechanisms for piezoelectric-based energy harvesters. *Energies*, 11(7):1850, 2018.
- [7] Ansys Inc. *Ansys fluent theory guide*, 2013.
- [8] Friedrich-Karl Benra, Hans Josef Dohmen, Ji Pei, Sebastian Schuster, and Bo Wan. A comparison of one-way and two-way coupling methods for numerical analysis of fluid-structure interactions. *Journal of applied mathematics*, 2011, 2011.
- [9] Alper Erturk and Daniel J Inman. *Piezoelectric energy harvesting*. John Wiley & Sons, 2011.
- [10] A Joly, S Etienne, and D Pelletier. Galloping of square cylinders in cross-flow at low reynolds numbers. *Journal of Fluids and Structures*, 28:232–243, 2012.
- [11] Alper Erturk, WGR Vieira, C De Marqui Jr, and Daniel J Inman. On the energy harvesting potential of piezoaeroelastic systems. *Applied physics letters*, 96(18):184103, 2010.
- [12] RWCP Verstappen and AEP Veldman. Fourth-order dns of flow past a square cylinder: First results. In *Direct and Large-Eddy Simulation II*, pages 381–384. Springer, 1997.
- [13] M Pourquie, M Breuer, and W Rodi. Computed test case: Square cylinder. In *Direct and Large-Eddy Simulation II*, pages 375–379. Springer, 1997.
- [14] Shingo Murakami and A Mochida. On turbulent vortex shedding flow past 2d square cylinder predicted by cfd. *Journal of Wind Engineering and Industrial Aerodynamics*, 54:191–211, 1995.
- [15] Kojiro Nozawa and Tetsuro Tamura. Les of flow past a square cylinder using embedded meshes. In *Direct and Large-Eddy Simulation II*, pages 409–412. Springer, 1997.
- [16] Norifusa Kawashima and Hiroshi Kawamura. Numerical analysis of les of flow past a long square cylinder. In *Direct and Large-Eddy Simulation II*, pages 413–422. Springer, 1997.
- [17] Dennis A Lyn, S Einav, W Rodi, and J-H Park. A laser-doppler velocimetry study of ensemble-averaged characteristics of the turbulent near wake of a square cylinder. *Journal of Fluid Mechanics*, 304:285–319, 1995.
- [18] DA Lyn and W Rodi. The flapping shear layer formed by flow separation from the forward corner of a square cylinder. *Journal of fluid Mechanics*, 267:353–376, 1994.
- [19] Jayant Sirohi and Rohan Mahadik. Harvesting wind energy using a galloping piezoelectric beam. *Journal of vibration and acoustics*, 134(1), 2012.